Gate-tunable spin waves in antiferromagnetic atomic bilayers

Xiao-Xiao Zhang[1,2], Lizhong Li[3], Daniel Weber[4], Joshua Goldberger[4], Kin Fai Mak[1,3,5*], Jie Shan[1,3,5*]

[1]Kavli Institute at Cornell for Nanoscale Science, Ithaca, New York, USA
[2]Department of Physics, University of Florida, Gainesville, Florida, USA
[3]School of Applied and Engineering Physics, Cornell University, Ithaca, New York, USA
[4]Department of Chemistry and Biochemistry, Ohio State University, Columbus, Ohio, USA
[5]Laboratory of Atomic and Solid State Physics, Cornell University, Ithaca, New York, USA
Email: kinfai.mak@cornell.edu; jie.shan@cornell.edu

Remarkable properties of two-dimensional (2D) layer magnetic materials, including spin filtering in magnetic tunnel junctions and gate control of magnetic states, have been recently demonstrated[1-12]. Whereas these studies have focused on static properties, dynamic magnetic properties such as excitation and control of spin waves have remained elusive. Here we investigate spin-wave dynamics in antiferromagnetic CrI_3 bilayers using an ultrafast optical pump/magneto-optical Kerr probe technique. Monolayer WSe_2 with strong excitonic resonance is introduced on CrI_3 to enhance optical excitation of spin waves. We identify sub-terahertz magnetic resonances under an in-plane magnetic field, from which the anisotropy and interlayer exchange fields are determined. We further show tuning of antiferromagnetic resonances by tens of gigahertz through electrostatic gating. Our results shed light on magnetic excitations and spin dynamics in 2D magnetic materials, and demonstrate their potential for applications in ultrafast data storage and processing.

Spin waves are propagating disturbances in magnetic ordering in a material. The quanta of spin waves are called magnons. The rich spin-wave phenomena in magnetic materials have attracted fundamental interest and impacted on technology of telecommunication systems, radars, and potentially also low-power information transmission and processing [13]. The main magnetic materials of interest have so far been ferromagnets. The operation speed of ferromagnet-based devices is limited by the ferromagnetic (FM) resonance frequency, which is typically in the GHz range. One of the major attractions of antiferromagnets, a class of much more common magnetic materials, is the prospect of high-speed operation. The antiferromagnetic (AF) resonances are in the frequency range of as high as THz because of the spin-sublattice exchange [14]. The antiferromagnets, however, are difficult to access due to the absence of macroscopic magnetization.

The recent discovery of two-dimensional (2D) layered magnetic materials [15-17], particularly A-type antiferromagnets, which are antiferromagnetically coupled FM layers [15], presents new opportunities to unlock the properties of antiferromagnets. With fully uncompensated FM surfaces, the magnetic state can be easily accessed and controlled [18]. These materials can be easily integrated into heterostructures with high-quality interfaces [19]. Their atomic thickness allows the application of strong electric field and large electrostatic doping to control the magnetic properties. Although rapid progress has been made in both fundamental understanding and potential applications [1-11], spin dynamics, including basic properties such as magnetic resonances and damping, have remained elusive in these atomically thin materials.

Here we investigate spin-wave excitations in bilayer CrI_3, a model A-type antiferromagnet, using the time-resolved magneto-optical Kerr effect (MOKE). Magnetic resonances have been recently studied in bulk layered magnets including CrI_3 and $CrCl_3$ by neutron scattering and microwave absorption [20-22]. But extending these conventional probes to atomically thin samples, whose typical lateral size is a few microns, is extremely difficult because of the small amount of spins. Raman spectroscopy[23-26] has been applied to few-layer CrI_3 and other layered magnetic materials, but accurate identification of magnetic resonances (which lie in the ultralow Raman frequencies) is challenging. The time-resolved MOKE can access small-size samples and a wide range of resonance frequencies, and is ideally suited for such a study.

The sample is a bilayer CrI_3/monolayer WSe_2 heterostructure. It is encapsulated in hexagonal boron nitride (hBN) thin layers for protection of air-sensitive CrI_3 (Fig. 1a, b). Whereas bulk CrI_3 is an FM semiconductor, bilayer CrI_3 is an AF semiconductor with a Néel temperature of about 45 K [15]. It consists of two antiferromagnetically coupled FM monolayers with out-of-plane anisotropy. Monolayer WSe_2 is a direct gap nonmagnetic semiconductor with strong spin-orbit interactions [27]. It has a type-II band alignment with CrI_3 [28] (Fig. 1c). As we discuss below, monolayer WSe_2 is introduced to significantly enhance the optical pump absorption and spin-wave excitation in CrI_3. It also breaks the layer symmetry in bilayer CrI_3 to allow the detection of different spin-wave modes in the polar MOKE geometry. Figure 1d is the magnetization of the heterostructure versus out-of-plane magnetic field at 4 K measured by magnetic circular dichroism (MCD) at 1.8 eV. The AF behavior is fully consistent with the reported results for bilayer CrI_3 [15]. The small nonzero magnetization at low fields is a manifestation of the broken layer symmetry. The sharp change of magnetization with hysteresis around 0.75 T corresponds to a spin-flip transition. It provides a measure of the interlayer exchange field H_E.

A pulsed laser (200-fs pulse duration) is employed for the time-resolved measurements. The heterostructure is excited by a light pulse centered around the WSe_2 fundamental exciton resonance (1.73 eV), and the change in CrI_3 magnetization is probed by a time-delayed pulse around 1.54 eV. Both the pump and probe are linearly polarized and at normal incidence. The pump-induced polarization rotation of the probe is detected. It is sensitive only to the out-of-plane component of the magnetization. We apply an in-plane magnetic field $\mu_0 H_\parallel$ (μ_0 denoting the vacuum permeability) to tilt the magnetization from the easy axis and monitor the spin precession dynamics. Unless otherwise specified, all measurements were performed at 1.7 K. (See Methods for details on the sample fabrication and the time-resolved MOKE setup.)

Figure 2a displays the time evolution of the pump-induced change in MOKE of bilayer CrI_3 under $H_\parallel$ ranging from 0 – 6 T. For all fields, the MOKE signal shows a sudden change at time zero, followed by an exponential decay on the scale of 10's – 100's ps. This reflects the incoherent demagnetization process, in which the magnetic order is disturbed instantaneously by the pump pulse and slowly goes back to equilibrium. Oscillations on the MOKE signal are also instantaneous. The amplitude, frequency and damping of the oscillations evolve systematically with $H_\parallel$.

Figure 2b is the fast Fourier transform (FFT) of the oscillatory part of the time traces after subtraction of the exponentially decaying demagnetization dynamics. At low $H_{\parallel}$, a resonance around 70 GHz is observed. As $H_{\parallel}$ increases, the resonance splits into two. The low-energy mode redshifts significantly and the high-energy one barely shifts until 3.3 T. Above this field, both modes blueshift with increasing $H_{\parallel}$. While the amplitude of the low-energy mode diminishes quickly, the amplitude of the high-energy mode does not depend strongly on field.

We perform a more detailed analysis of the MOKE dynamics directly in the time domain by fitting them with two damped harmonic waves (red lines, Fig. 3a). Two sample time traces (after subtraction of the demagnetization dynamics) are shown for $H_{\parallel}$ at 1.5 and 3.75 T. The extracted resonance frequencies, damping rates and amplitudes versus $H_{\parallel}$ of these two modes are summarized in Fig. 3c, 3d and Supplementary Fig. S8, respectively. The results are in good agreement with peak fittings to the FFT spectra (Fig. 2b and Supplementary Fig. S9). We first focus on the resonance frequencies. The field dependence of the modes (ω_h for high-energy mode and ω_l for the low-energy mode) shows two distinct regimes. Below about 3.3 T, the two initially degenerate modes split. While both modes soften with increasing field, the low-energy mode drops nearly to zero frequency. Above 3.3 T, both modes show a linear increase in frequency with a slope equal to the electron gyromagnetic ratio $\gamma/2\pi \approx 28$ GHz/T. The latter is characteristic of a FM resonance in high fields.

The observed field dispersion of the modes is indicative of their magnon origin with a saturation field $H_S \approx 3.3$ T (the field required to fully align the magnetization in-plane) [8]. The two modes are the spin precession eigenmodes of the coupled top- and bottom-layer magnetizations under $H_{\parallel}$ (Fig. 3b). Above H_S, the spins are aligned in-plane and the spin waves become FM-like. This interpretation is further supported by the temperature dependence of the resonances (Supplementary Fig. S4-6). Clear mode softening is observed with increasing temperature and the resonance feature disappears near the Néel temperature.

We briefly consider the microscopic mechanism for the observed ultrafast excitation of spin waves in bilayer CrI_3 (see Methods for more discussions). The most plausible process involves exciton generation in WSe_2 by the optical pump, followed by ultrafast exciton dissociation and electron transfer at the CrI_3-WSe_2 interface [28], and an impulsive perturbation to the magnetic interactions [29] in CrI_3 by the hot carriers (Fig. 1c). This picture is supported by several control experiments, particularly the pump wavelength dependence of the spin-wave amplitude, which agrees with the WSe_2 absorption spectrum (Supplementary Fig. S1). We have also obtained results on a thicker CrI_3 sample without WSe_2 layer (Supplementary Fig. S10), in which the MOKE signal is weaker than bilayer CrI_3, illustrating the importance of WSe_2 enhancement. Other possible processes such as photon angular momentum transfer and thermal effects have also been considered. The lack of pump polarization dependence (Supplementary Fig. S2) and the instantaneous excitation of the spin waves (Fig. 2a) exclude these processes.

We model the field-dependent spin-wave dynamics using the coupled Landau-Lifshitz-Gilbert (LLG) equations. They describe precession of antiferromagnetically coupled top- and bottom-layer magnetizations under $H_{\parallel}$ (Details are provided in Methods) [30]. The effective magnetic field at each layer includes contributions from the applied field $H_{\parallel}$, intralayer anisotropy field H_A, and interlayer exchange field H_E. In the simple case of negligible damping and symmetric layers, the precession eigenmode frequencies are found to be $\omega_h = \gamma\left[H_A(2H_E + H_A) + \frac{2H_E - H_A}{2H_E + H_A}H_{\parallel}^2\right]^{\frac{1}{2}}$, $\omega_l = \gamma\left[H_A(2H_E + H_A) - \frac{H_A}{2H_E + H_A}H_{\parallel}^2\right]^{\frac{1}{2}}$ (before saturation), and $\omega_h = \gamma\sqrt{H_{\parallel}(H_{\parallel} - H_A)}$, $\omega_l = \gamma\sqrt{(H_{\parallel} - 2H_E)(H_{\parallel} - 2H_E - H_A)}$ (after saturation). The low-energy mode ω_l corresponds to the net moment oscillations along the applied field (the y-axis). It drops to zero at the saturation field $H_S = 2H_E + H_A$. The high-energy mode ω_h corresponds to the net moment oscillations in the x-z plane (Fig. 3b).

The simple solution describes the experimental result well for the entire field range (dashed lines, Fig. 3c) with $H_A \approx 1.77$ T and $H_E \approx 0.76$ T. Since $H_A > H_E$, a spin-flip transition is expected under a field along the easy axis (Fig. 1d) [30]. The extracted H_E is in good agreement with the observed spin-flip transition field [30]. The saturation field evaluated from H_A and H_E ($H_S \approx 3.3$ T, vertical dotted lines in Fig. 3c, d) is slightly below the reported value for bilayer CrI_3 (3.8 T at 2 K) [8]. This could arise from the different doping levels in different samples (Fig. 4c). The extracted H_A is smaller than the bulk value (~ 2.5 T) [23], which is consistent with the lower magnetic transition temperature observed in atomically thin samples than in bulk samples [15].

We examine the normalized damping rate $(2\pi/\omega\tau)$ of the modes as a function of $H_{\parallel}$ in Fig. 3d. Overall, damping is higher below or near saturation. In this regime, the mode frequencies are strongly dependent on internal magnetic interactions, which are prone to local doping and strain. Inhomogeneous broadening of the magnetic resonances and spin-wave dephasing is thus likely the dominant damping mechanism. For instance, a variation in H_E at the 10% level (typical for bilayer CrI_3 [3]) could account for the observed damping rate for the high-energy mode below H_S. Inhomogeneous broadening also explains the seemingly higher damping for the low-energy mode near H_S since its frequency has a steeper dispersion with $H_{\parallel}$ near H_S. Above saturation, the mode frequencies are basically determined by the applied field. Inhomogeneous broadening becomes insignificant especially in the high-field limit (e.g. at 6 T). Our observation of weak layer number dependence of damping from experiment on few-layer CrI_3 (Supplementary Fig. S10) suggests that interfacial damping is also not significant. More systematic studies are required to identify the dominant damping mechanism in this regime.

Finally we demonstrate control of the spin waves by electrostatic gating using a dual-gate device (Fig. 1b). Equal top and bottom gate voltages are applied to the two symmetric gates to induce doping in the heterostructure (see Methods for details). Figure 4a shows the FFT amplitude spectra of coherent spin oscillations under an in-plane field of 2 T at different gate voltages. The high-energy mode shifts continuously from ~ 80 GHz to ~ 55 GHz when the gate voltage is varied from -13 V to +13 V (corresponding to from 'hole doping' to 'electron doping'). Figure 4b shows the magnetic-field dispersion of the high-energy mode (symbols) at representative gate voltages (the low-energy mode is not studied because of its small amplitude). Similar to the zero-gate voltage case, they all show an initial redshift followed by a blueshift with increasing $H_{\parallel}$. The turning point (i.e. the saturation field) is varied by as much as 1 T. The mode dispersion is strongly modified by gating below saturation and remains nearly unchanged above it.

The observed mode dispersion at different gate voltages can also be described by the above simple solution of the LLG equations (solid lines, Fig. 4b). The corresponding interlayer exchange and intralayer anisotropy fields in the model are shown in Fig. 4c as a function of gate voltage. Both decrease linearly with increasing gate voltage, with H_A at a higher rate than H_E. Similar gate dependence for H_E has been reported from the study of the spin-flip transition under an out-of-plane field in bilayer CrI_3 [6]. The effect can be understood as a consequence of doping dependent electron occupancy of the magnetic Cr^{3+} ions and their wavefunction overlap. Increasing electron density weakens the magnetic interactions and the applied field responsible for spin precession below H_S. Above H_S, the magnetization is fully saturated in-plane. The mode frequency is mainly determined by the applied field and is nearly doping independent. However, a quantitative description of the experimental result would require *ab initio* calculations and is beyond the scope of the current study.

In conclusion, we have demonstrated generation, detection, and gate-tuning of spin waves in a model 2D antiferromagnet bilayer CrI_3. Our results allow the characterization of internal magnetic interactions and damping. The combination of the time-resolved MOKE and type-II heterostructures that facilitate ultrafast interlayer charge transfer for efficient spin-wave excitation can be applied to a broad class of magnetic thin films. Local gate control of spin dynamics may also have implications for reconfigurable spin-based devices.

References

1 Gibertini, M., Koperski, M., Morpurgo, A. F. & Novoselov, K. S. Magnetic 2D materials and heterostructures. *Nature Nanotechnology* **14**, 408-419, (2019).

2 Gong, C. & Zhang, X. Two-dimensional magnetic crystals and emergent heterostructure devices. *Science* **363**, eaav4450, (2019).

3 Mak, K. F., Shan, J. & Ralph, D. C. Probing and controlling magnetic states in 2D layered magnetic materials. *Nature Reviews Physics* **1**, 646-661, (2019).

4 Burch, K. S., Mandrus, D. & Park, J.-G. Magnetism in two-dimensional van der Waals materials. *Nature* **563**, 47-52, (2018).

5 Jiang, S., Shan, J. & Mak, K. F. Electric-field switching of two-dimensional van der Waals magnets. *Nature Materials* **17**, 406-410, (2018).

6 Jiang, S., Li, L., Wang, Z., Mak, K. F. & Shan, J. Controlling magnetism in 2D CrI3 by electrostatic doping. *Nature Nanotechnology* **13**, 549-553, (2018).

7 Huang, B. *et al.* Electrical control of 2D magnetism in bilayer CrI3. *Nature Nanotechnology* **13**, 544-548, (2018).

8 Song, T. *et al.* Giant tunneling magnetoresistance in spin-filter van der Waals heterostructures. *Science* **360**, 1214, (2018).

9 Klein, D. R. *et al.* Probing magnetism in 2D van der Waals crystalline insulators via electron tunneling. *Science* **360**, 1218, (2018).

10 Song, T. *et al.* Voltage Control of a van der Waals Spin-Filter Magnetic Tunnel Junction. *Nano Letters* **19**, 915-920, (2019).

11 Wang, Z. *et al.* Very large tunneling magnetoresistance in layered magnetic semiconductor CrI3. *Nature Communications* **9**, 2516, (2018).

12 Kim, H. H. *et al.* One Million Percent Tunnel Magnetoresistance in a Magnetic van der Waals Heterostructure. *Nano Letters* **18**, 4885-4890, (2018).

13 Chumak, A. V., Vasyuchka, V. I., Serga, A. A. & Hillebrands, B. Magnon spintronics. *Nature Physics* **11**, 453-461, (2015).
14 Baltz, V. *et al.* Antiferromagnetic spintronics. *Reviews of Modern Physics* **90**, 015005, (2018).
15 Huang, B. *et al.* Layer-dependent ferromagnetism in a van der Waals crystal down to the monolayer limit. *Nature* **546**, 270, (2017).
16 Gong, C. *et al.* Discovery of intrinsic ferromagnetism in two-dimensional van der Waals crystals. *Nature* **546**, 265, (2017).
17 Deng, Y. *et al.* Gate-tunable room-temperature ferromagnetism in two-dimensional Fe3GeTe2. *Nature* **563**, 94-99, (2018).
18 Duine, R. A., Lee, K.-J., Parkin, S. S. P. & Stiles, M. D. Synthetic antiferromagnetic spintronics. *Nature Physics* **14**, 217-219, (2018).
19 Novoselov, K. S., Mishchenko, A., Carvalho, A. & Castro Neto, A. H. 2D materials and van der Waals heterostructures. *Science* **353**, aac9439, (2016).
20 MacNeill, D. *et al.* Gigahertz Frequency Antiferromagnetic Resonance and Strong Magnon-Magnon Coupling in the Layered Crystal ${\mathrm{CrCl}}_{3}$. *Physical Review Letters* **123**, 047204, (2019).
21 Lee, I. *et al.* Fundamental Spin Interactions Underlying the Magnetic Anisotropy in the Kitaev Ferromagnet ${\mathrm{CrI}}_{3}$. *Physical Review Letters* **124**, 017201, (2020).
22 Chen, L. *et al.* Topological Spin Excitations in Honeycomb Ferromagnet ${\mathrm{CrI}}_{3}$. *Physical Review X* **8**, 041028, (2018).
23 Lee, J.-U. *et al.* Ising-Type Magnetic Ordering in Atomically Thin FePS3. *Nano Letters* **16**, 7433-7438, (2016).
24 Jin, W. *et al.* Raman fingerprint of two terahertz spin wave branches in a two-dimensional honeycomb Ising ferromagnet. *Nature Communications* **9**, 5122, (2018).
25 Cenker, J. *et al.* Direct observation of 2D magnons in atomically thin CrI $ _3$. *arXiv preprint arXiv:2001.07025*, (2020).
26 McCreary, A. *et al.* Quasi-two-dimensional magnon identification in antiferromagnetic $\mathrm{FeP}{\mathrm{S}}_{3}$ via magneto-Raman spectroscopy. *Physical Review B* **101**, 064416, (2020).
27 Wang, G. *et al.* Colloquium: Excitons in atomically thin transition metal dichalcogenides. *Reviews of Modern Physics* **90**, 021001, (2018).
28 Zhong, D. *et al.* Van der Waals engineering of ferromagnetic semiconductor heterostructures for spin and valleytronics. *Science Advances* **3**, e1603113, (2017).
29 Kirilyuk, A., Kimel, A. V. & Rasing, T. Ultrafast optical manipulation of magnetic order. *Reviews of Modern Physics* **82**, 2731-2784, (2010).
30 Gurevich, A. G. & Melkov, G. A. *Magnetization oscillations and waves*. (CRC press, 1996).

Methods

Sample and device fabrication

The measured sample is a stack of 2D materials composed of (from top to bottom) few-layer graphite, hBN, monolayer WSe_2, bilayer CrI_3, hBN, and few-layer graphite (Fig. 1b). The top and bottom graphite/hBN pairs serve as gates. An additional stripe of graphite is attached to the WSe_2 flake for grounding and charge injection. The thickness of hBN layers is ~ 30 nm, and the graphite layers, about 2-6 nm. All layer materials were first exfoliated from their bulk crystals onto SiO_2/Si substrates and identified by their color contrast under an optical microscope. The heterostructure was built by the layer-by-layer dry transfer technique [31]. It was then released onto a substrate with pre-patterned gold electrodes, which contact the bottom gate, top gate, and grounding graphite flake. The steps involving CrI_3 before its full encapsulation in hBN layers were performed inside a nitrogen-filled glovebox because CrI_3 is air sensitive.

Bulk crystals of graphite, hBN and WSe_2 were from HQ graphene. Bulk CrI_3 crystals were synthesized by chemical vapor transport following methods described in previous reports[32,33]. They crystallize into the $C2/m$ space group with typical lattice constants of $a = 6.904$ Å, $b = 11.899$ Å, $c = 7.008$ Å and $\beta = 108.74°$, and Curie temperatures of 61 K.

In the gating experiment, equal top and bottom gate voltages of the same sign were applied to the two nearly symmetric gates. The gate voltage shown in Fig. 4 is the voltage on each gate. This geometry allows electrostatic doping into the heterostructure without introducing a vertical electric field[34]. The total carrier density in the CrI_3-WSe_2 heterostructure can be calculated from the gate voltage and the gate capacitances [6]. Because CrI_3 has a much higher density of states than WSe_2, majority of the gate-induced carriers goes into the CrI_3 layer. We measured the doping density in the WSe_2 layer independently by monitoring the photoluminescence energy of charged excitons (trions), which is a sensitive function of doping density [35]. Doping density in CrI_3 was obtained by subtracting the carrier density in WSe_2 from the total carrier density. Supplementary Figure S3 shows Fig. 4c with the calibrated doping density in CrI_3 shown in the top axis.

Time-resolved magneto-optical Kerr effect (MOKE) and magnetic circular dichroism (MCD)

In the time-resolved MOKE setup, the probe beam is the output of a Ti:Sapphire oscillator (Coherent Chameleon with a repetition rate of 78 MHz and pulse duration of 200 fs) centered at 1.54 eV, and the pump beam is the second harmonic of an optical parametric oscillator (OPO) (Coherent Chameleon compact OPO) output centered at 1.73 eV. The time delay between the pump and probe pulses is controlled by a motorized linear delay stage. Both the pump and probe beam are linearly polarized. The pump intensity is modulated at 100 kHz by a combination of a half-wave photoelastic modulator (PEM) and a linear polarizer whose transmission axis is perpendicular to the original pump polarization. The pump and probe beam impinge on the sample at normal incidence. The reflected light is first filtered to remove the pump, passed through a half-wave Fresnel rhomb and a Wollaston prism, and detected by a pair of balanced photodiodes. The pump-induced change in Kerr rotation is determined as the ratio of the intensity imbalance of the photodiodes obtained from a lock-in amplifier locked at the pump modulation frequency and the intensity of each photodiode.

For the MCD measurements, a single beam centered at 1.8 eV is used. The light beam is modulated at 50 kHz between the left and right circular polarization using a PEM. The reflected light is focused onto a photodiode. The MCD is determined as the ratio of the ac component of the photodiode signal measured by a lock-in amplifier at the polarization modulation frequency and the dc component of the photodiode signal measured by a voltmeter.

For all measurements samples were mounted in an optical cryostat (attoDry2100) with a base temperature of 1.7 K and a superconducting solenoid magnet up to 9 Tesla. For measurements under an out-of-plane field, the sample was mounted horizontally and light was focused onto the sample at normal incidence by a microscope objective. For measurements under an in-plane field, the sample was mounted vertically and the light beam was guided by a mirror at 45° and focused onto the sample at normal incident by a lens.

Landau-Lifshitz-Gilbert (LLG) equations

We model the field-dependent spin dynamics in AF bilayer CrI_3 using coupled Landau-Lifshitz-Gilbert (LLG) equations [30],

$$\frac{\partial \boldsymbol{M}_i}{\partial t} = -\gamma \boldsymbol{M}_i \times \boldsymbol{H}_i^{eff} + \frac{\alpha}{M_S} \boldsymbol{M}_i \times \frac{\partial \boldsymbol{M}_i}{\partial t}. \tag{1}$$

Here $\boldsymbol{M}_i$ (i = 1, 2) is the magnetization of the top or bottom layer (which is assumed to have a magnitude M_S), $\gamma/2\pi \approx 28$ GHz/T is the electron gyromagnetic ratio, α is the dimensionless damping factor, and $\boldsymbol{H}_i^{eff}$ is the effective magnetic field at the i-th layer that is responsible for spin precession. In the absence of applied magnetic field, $\boldsymbol{M}_1$ and $\boldsymbol{M}_2$ are anti-aligned along the easy axis (z-axis). When an in-plane field $\boldsymbol{H}_\parallel$ (along the y-axis) is applied, $\boldsymbol{M}_1$ and $\boldsymbol{M}_2$ are tilted symmetrically towards the y-axis, before fully turned into the applied field direction at the saturation field $H_S = 2H_E + H_A$. Here H_E and H_A are the interlayer exchange and intralayer anisotropy fields, respectively. The canting angle θ of magnetization (with respect to the anisotropy axis) is given by $\sin\theta = H_\parallel/H_S$ (Supplementary Fig. S11). The effective field has contributions from the applied field, the interlayer exchange field, and the intralayer anisotropy field $\boldsymbol{H}_{1,2}^{eff} = \boldsymbol{H}_\parallel - \frac{H_E}{M_S}\boldsymbol{M}_{2,1} + \frac{H_A}{M_S}\left(\boldsymbol{M}_{1,2}\right)_z \hat{\boldsymbol{z}}$. We search for solution in the form of a harmonic wave $e^{i\omega t}$ with angular frequency ω. For the simple case of zero damping (α = 0), two eigenmode frequencies ($\omega_h \geq \omega_l$) are given in the main text.

In case of finite but weak damping, we simplify the LLG equations for the high-energy and low-energy modes. Before saturation ($H_\parallel < H_S$),

$$\omega_h^2(1+\alpha^2) - i\alpha\omega_h\gamma\left(\frac{\omega_{h0}^2/\gamma^2}{2H_E+H_A} + 2H_E + H_A\right) - \omega_{h,0}^2 = 0; \tag{2}$$

$$\omega_l^2(1+\alpha^2) - i\alpha\omega_l\gamma\left(\frac{\omega_{l0}^2/\gamma^2}{H_A} + H_A\right) - \omega_{l,0}^2 = 0. \tag{3}$$

After saturation ($H_\parallel > H_S$),

$$\omega_h^2(1+\alpha^2) - i\alpha\omega_h\gamma(2H_\parallel - H_A) - \omega_{h,0}^2 = 0; \tag{4}$$

$$\omega_l^2(1+\alpha^2) - i\alpha\omega_l\gamma(2H_\parallel - 4H_E - H_A) - \omega_{l,0}^2 = 0. \tag{5}$$

Here $\boldsymbol{\omega_{h,0}}$ and $\boldsymbol{\omega_{l,0}}$ correspond to the solution at zero damping ($\boldsymbol{\alpha}$ = 0). If $\boldsymbol{\alpha} << 1$, the oscillation frequency (the real part of $\boldsymbol{\omega_h}$ and $\boldsymbol{\omega_l}$) becomes $\frac{\boldsymbol{\omega_0}}{\sqrt{1+\alpha^2}}$, where $\boldsymbol{\omega_0}$ is the undamped solution for the two modes. With the correction from finite but very small $\boldsymbol{\alpha}$, the eigenmode frequencies are reduced, and the two modes are no longer degenerate at zero field.

Mechanism for ultrafast excitation of coherent magnons

We have investigated the mechanism for the observed ultrafast excitation of magnons in bilayer CrI_3. A plausible picture involves exciton generation in WSe_2 by the optical pump, ultrafast exciton dissociation and charge transfer at the CrI_3-WSe_2 interface, and an impulsive perturbation to the magnetic anisotropy and exchange fields in CrI_3 by the injected hot carriers. For a typical pump power used in the experiment and assuming ~20% WSe_2 light absorption at the pump energy, we estimate a transferred charge density of ~ 10^{12} cm^{-2} at time zero for 10 % charge transfer efficiency from WSe_2 to CrI_3. Such a density is on par with the electrostatic doping density that induces significant changes in the magnetic interactions (Supplementary Fig. S3).

Several control experiments were performed to test this picture. Pump-probe measurements were performed on both monolayer WSe_2 and bilayer CrI_3 areas alone (non-overlapped regions in the heterostructure) under the same experimental conditions. Negligible pump-induced MOKE signal was observed. Measurements were also done on the heterostructure at different pump energies. The mode frequencies were found unchanged, but the amplitudes are consistent with the absorption spectrum of WSe_2 (Supplementary Fig. S1). These two experiments show that magnons are generated through optical excitation of excitons in WSe_2. It has been reported that CrI_3-WSe_2 heterostructures have a type-II band alignment, which can facilitate ultrafast exciton dissociation and charge transfer at the interface [28]. Moreover, the onset of coherent oscillations is instantaneous with optical excitation. This excludes lattice heating in CrI_3 as a dominant mechanism for the generation of magnons, which typically takes a longer time to build up. Moreover, the resonance amplitude is independent of the pump laser polarization (Supplementary Fig. S2). It indicates that hot carriers, rather than the angular momentum of the carriers, are responsible for the excitation of magnons. These experiments are all consistent with the proposed mechanism of ultrafast excitations of magnons in CrI_3-WSe_2 heterostructures.

Temperature dependence of magnon modes

We have performed the optical pump/MOKE probe experiment in CrI_3-WSe_2 heterostructures at temperature ranging from 1.7 K to 50 K. No obvious oscillations can be measured above 50 K when bilayer CrI_3 is close to its Néel temperature (~ 45 K). The results at 1.7 K are presented in the main text. Supplementary Fig. S4 and S5 show the corresponding measurements and analysis for 25 K and 45 K, respectively. With increasing temperature, the magnon frequency decreases and the saturation field (estimated from the minimum of the frequency dispersion) decreases. A systematic temperature dependence is shown in Supplementary Fig. S6 for the high-energy mode ω_h at a fixed in-plane field of 2 T. The frequency has a negligible temperature dependence well below the Néel temperature (< 20 K), and decreases rapidly when the temperature approaches the Néel temperature.

Magnetic-field dependence of mode amplitudes

The magnetic-field dependence of the high-energy and low-energy mode amplitudes (Supplementary Fig. S8) can be qualitatively understood. Under zero magnetic field, the equilibrium magnetization is in the out-of-plane direction. Assuming that the magnetization amplitudes does not change, the out-of-plane magnetization oscillation is zero for both modes. With an increasing in-plane field, spins cant towards the in-plane direction, and the out-of-plane magnetization oscillation grows till the field reaches the saturation field. At this point, the magnetizations are fully aligned in-plane. With a further increase in the in-plane field, spins stiffen and the oscillation amplitude decreases. However, many details of Supplementary Fig. S8 remain not understood. For instance, the maximum amplitude of the two modes occurs at different in-plane fields, and the amplitude of the low-energy mode decreases much faster than the high-energy mode above saturation. Future systematic studies are required to better understand the field dependence of the mode amplitudes.

Measurements on few-layer CrI_3

We have measured the magnetic response from a few-layer CrI_3 (6-8 layer) sample. Because of the larger MOKE signal and higher optical absorption in thicker samples, magnetic oscillations can be measured without the enhancement from monolayer WSe_2. The results are shown in Supplementary Fig. S10. The comparison of results from samples of different thicknesses provides insight into the origin of magnetic damping. For instance, in the high-field limit (6 T), few-layer and bilayer CrI_3 show a similar level of damping. This indicates that interfacial damping is not the dominant contributor to damping.

Methods references

31 Wang, L. *et al.* One-Dimensional Electrical Contact to a Two-Dimensional Material. *Science* **342**, 614, (2013).

32 Shcherbakov, D. *et al.* Raman Spectroscopy, Photocatalytic Degradation, and Stabilization of Atomically Thin Chromium Tri-iodide. *Nano Letters* **18**, 4214-4219, (2018).

33 Li, T. *et al.* Pressure-controlled interlayer magnetism in atomically thin CrI3. *Nature Materials* **18**, 1303-1308, (2019).

34 Wang, Z., Chiu, Y.-H., Honz, K., Mak, K. F. & Shan, J. Electrical Tuning of Interlayer Exciton Gases in WSe2 Bilayers. *Nano Letters* **18**, 137-143, (2018).

35 Wang, Z., Zhao, L., Mak, K. F. & Shan, J. Probing the Spin-Polarized Electronic Band Structure in Monolayer Transition Metal Dichalcogenides by Optical Spectroscopy. *Nano Letters* **17**, 740-746, (2017).

Data availability

The data that support the findings of this study are available within the paper and its Supplementary Information. Additional data are available from the corresponding authors upon request.

Acknowledgments

This work was supported by the National Science Foundation under award DMR-1807810 (time-resolved spectroscopy), the Center for Emergent Materials: an NSF MRSEC under award number DMR-1420451 (bulk CrI_3 crystal growth and device fabrication), and the Air Force Office of Scientific Research under award number FA9550-19-1-0390 (data analysis). This work was also partially supported by the Cornell Center for Materials Research with funding from the NSF MRSEC program under DMR-1719875 (optical characterization). The growth of hBN crystals was supported by the Elemental Strategy Initiative conducted by the MEXT, Japan and the CREST(JPMJCR15F3), JST. D.W. gratefully acknowledges the financial support by the German Science Foundation (Deutsche Forschungsgemeinschaft, DFG) under the fellowship number WE6480/1. X.Z. acknowledges Postdoctoral Fellowship from the Kavli Institute at Cornell (KIC). K.F.M. acknowledges support from David and Lucille Packard Fellowship.

Author contributions

X.Z., K.F.M. and J.S. designed the study. X.Z. developed the time-resolved spectroscopy setup and performed the measurements. L.L. fabricated the devices and assisted X.Z. in the measurements. D.W. and J.E.G. grew the bulk CrI_3 crystals. K.W. and T.T. grew the bulk hBN crystals. X.Z., K.F.M. and J.S. co-wrote the manuscript. All authors discussed the results and commented on the manuscript.

Competing interests

The authors declare no competing interests.

Figure captions

Figure 1 | Bilayer CrI_3/monolayer WSe_2 heterostructures. a, Optical microscope image of the heterostruture. Bilayer CrI_3 is outlined with a purple line, monolayer WSe_2 with a black line, and one graphite gate layer with a gray line. The CrI_3/WSe_2 stack is encapsulated by hBN on both sides, and graphite layers are used to electrically connect to the lithographically defined metal electrodes (bottom and top right). The dark spots are air bubbles trapped in the 2D stack. Scale bar is 5 μm. **b,** Schematic sideview of the dual-gated device employed in the gating experiment. **c**, Schematic of a type-II band alignment between monolayer WSe_2 and CrI_3. Optically excited exciton in WSe_2 is dissocated at the interface and electron is transferred to CrI_3 [28]. **d,** Magnetic circular dichroism (MCD) of the heterostrucutre as a function of out-of-plane magnetic field ($\mu_0 H_\perp$) at 4 K. Hysteresis is observed for field sweeping along two opposing directions. Insets are schematics of the corresponding magnetization in the top and bottom layers of blayer CrI_3. The dashed lines indicate the spin-flip transition around 0.75 T.

Figure 2 | Time-resolved magnon oscillations. a, Pump-induced Kerr rotation as a function of pump-probe delay time in bilayer CrI_3 under different in-plane magnetic fields. **b,** Fast Fourier transform **(**FFT) amplitude spectra of the time dependences shown in **a** after the removal of the demagnetization dynamics (exponential decay). The black dashed lines are Voigt peak fitting of the resonance features centered at frequencies of Fig. 3c. The curves in **a** and **b** are vertically displaced for clarity. The keys between the panels are for both panels.

Figure 3 | Magnon dispersion and damping. a, Pump-induced magneto-optical Kerr effect (MOKE) dynamics in bilayer CrI_3 under two representative in-plane fields of 1.5 T (upper panel) and 3.75 T (lower panel). Grey lines are experiment after subtracting the demagnetization dynamics, and red lines, fits to two damped harmonic oscillations. **b,** Illustration of two spin-wave eigenmodes under an in-plane field (y-axis): the high-energy mode (left) and the low-energy mode (right). The dotted lines indicate the equilibrium top and bottom layer magnetization M_1 and M_2, which are titled symmetrically from the z-axis towards the applied field. The magnetizations precess following the green and blue arrows in the order 1 through 4. **c, d,** Magnetic-field dependence of frequencies (**c**) and damping rates (**d**) of the high-energy and low-energy modes extracted from the fit shown in **a**. The damping coefficient $\alpha = 2\pi/\omega\tau$ is normalized by the resonance frequency ω. The error bars are the fit uncertainties. Dashed lines in **c** are fits to the Landau-Lifshitz-Gilbert (LLG) equations as described in the text. The vertical dotted lines indicate the in-plane saturation field from the fits to the LLG equations.

Figure 4 | Gate tunable magnon frequencies. a, Fast Fourier transform (FFT) amplitude spectra of the magnons as a function of gate voltage under a fixed in-plane field of 2 T. Dashed lines are Voigt peak fits. The gray line is a guide to the eye of the evolution of the mode frequency with gate voltage and triangles indicate the peak of the resonance. **b,** Magnetic-field dispersion of the high-energy mode at representative gate voltages. The solid lines are fits to the Landau-Lifshitz-Gilbert (LLG) equations and symbols are experimental data. Fig. S12 shows the magnetic dispersion for the measured gate voltages in **a.** **c,** Anisotropy and exchange field extracted from the fits in **b** at different gate voltages. Error bars are the standard deviation from the fitting. Dashed lines are linear fits.

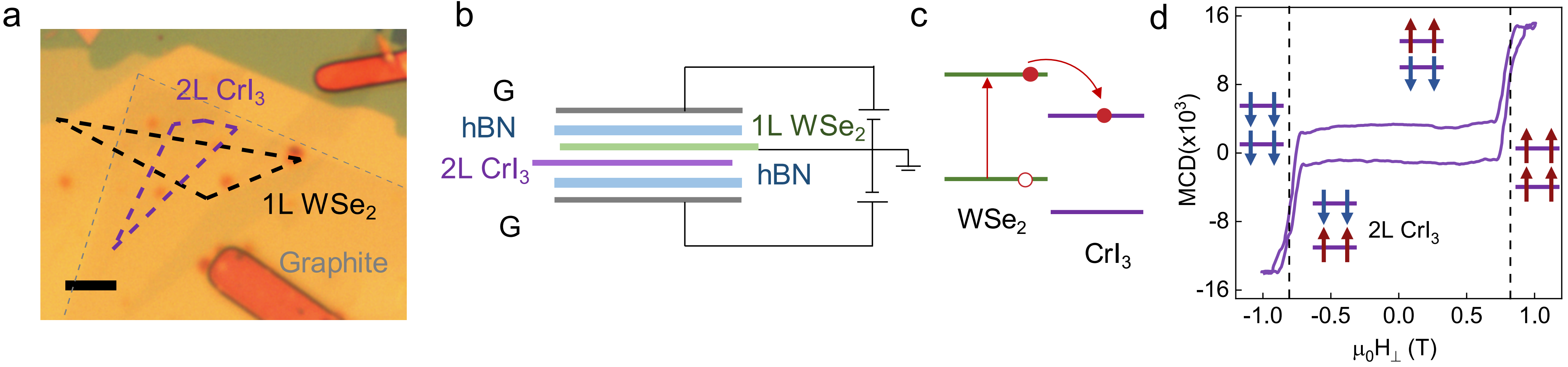
a
2L CrI3
1L WSe2
Graphite
b
G
hBN
1L WSe2
2L CrI3
hBN
G
c
WSe2
CrI3
d
MCD(x10^3)
16
8
0
-8
-16
2L CrI3
-1.0
-0.5
0.0
0.5
1.0
μ0H⊥ (T)

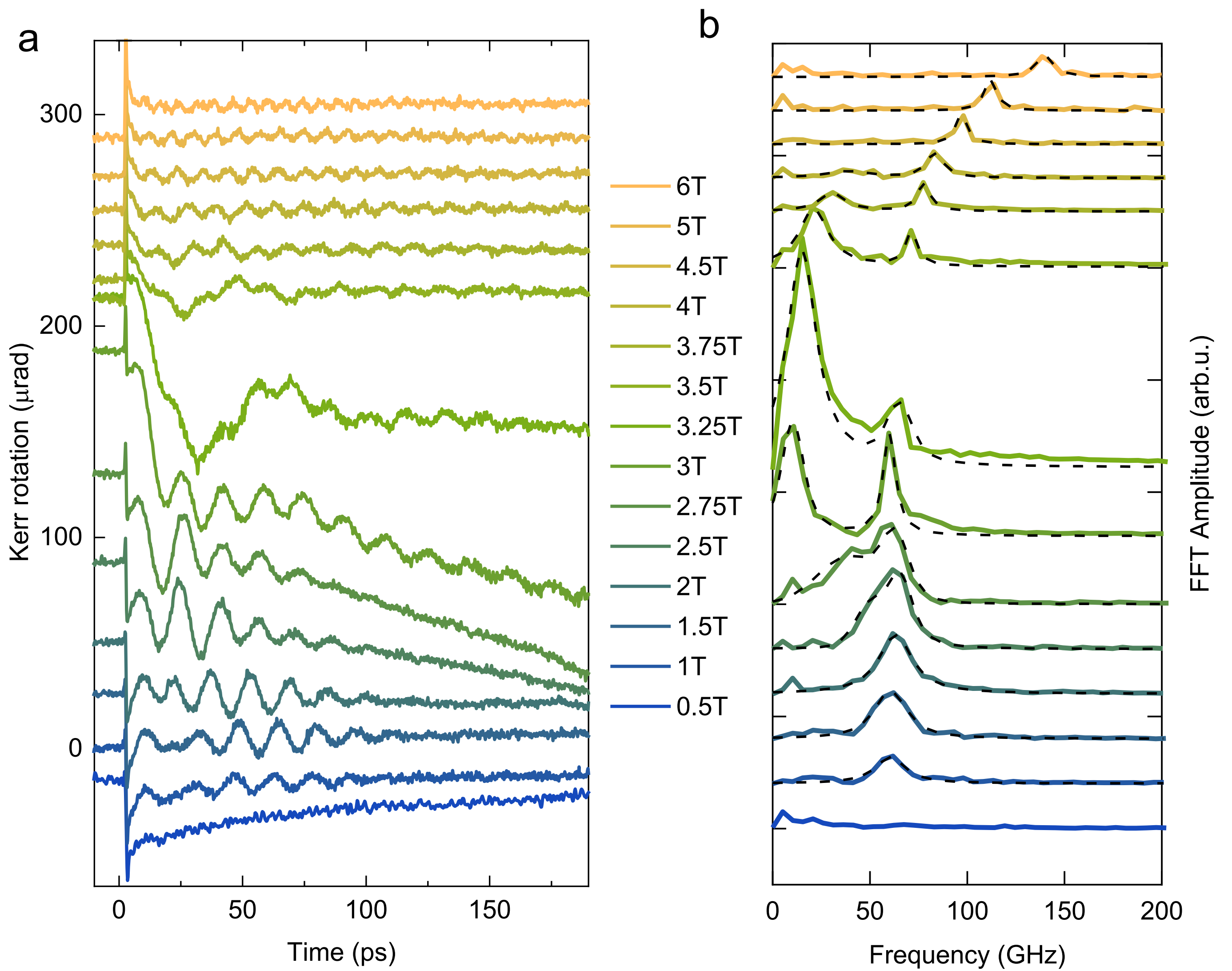
a
b
Kerr rotation (μrad)
300
200
100
0
0
50
100
150
Time (ps)
6T
5T
4.5T
4T
3.75T
3.5T
3.25T
3T
2.75T
2.5T
2T
1.5T
1T
0.5T
FFT Amplitude (arb.u.)
0
50
100
150
200
Frequency (GHz)

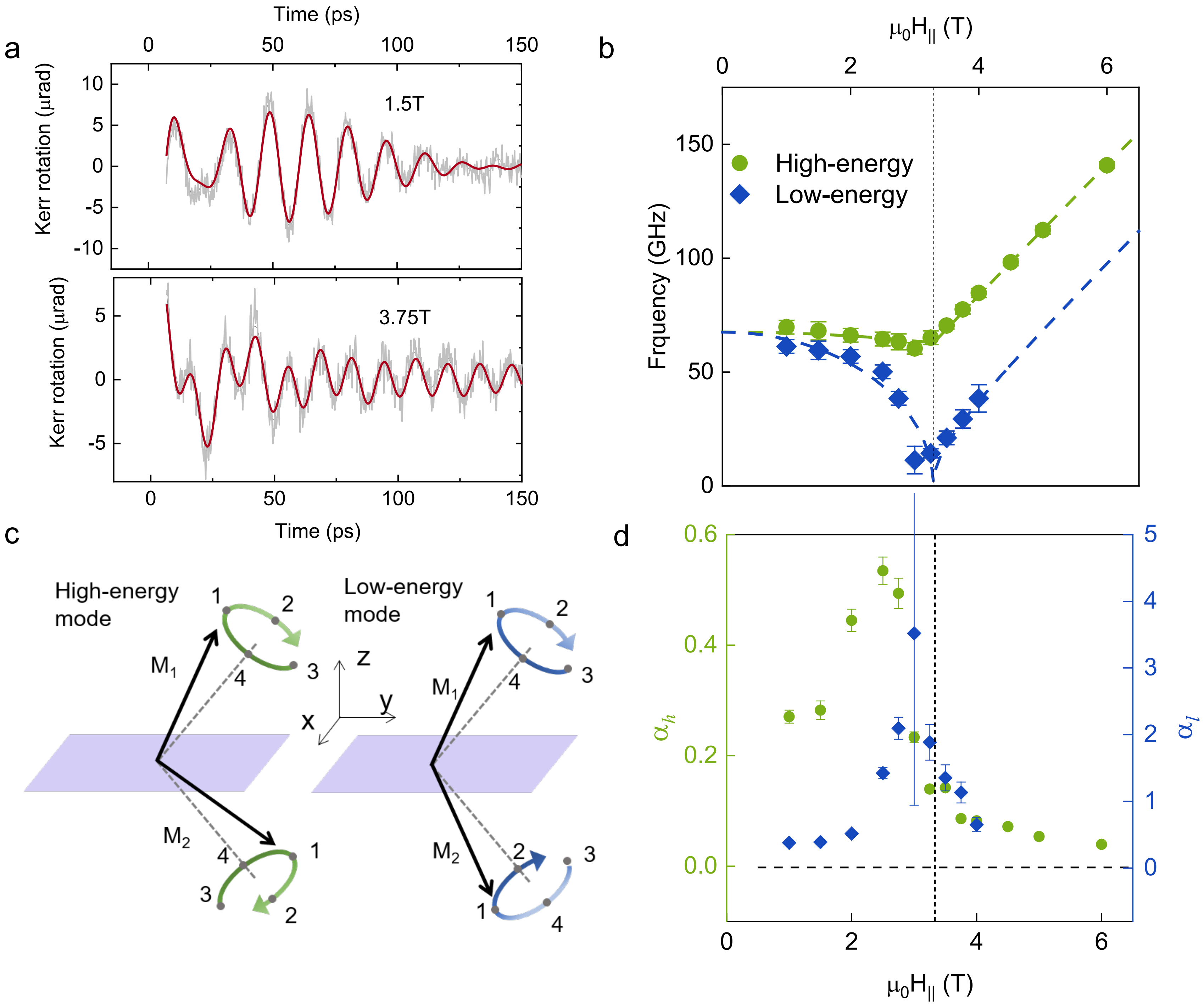

a
Time (ps)
Kerr rotation (μrad)
1.5T
3.75T
b
$\mu_0 H_{||}$ (T)
Frquency (GHz)
High-energy
Low-energy
c
High-energy mode
Low-energy mode
M_1
M_2
z
y
x
d
α_h
α_l
$\mu_0 H_{||}$ (T)

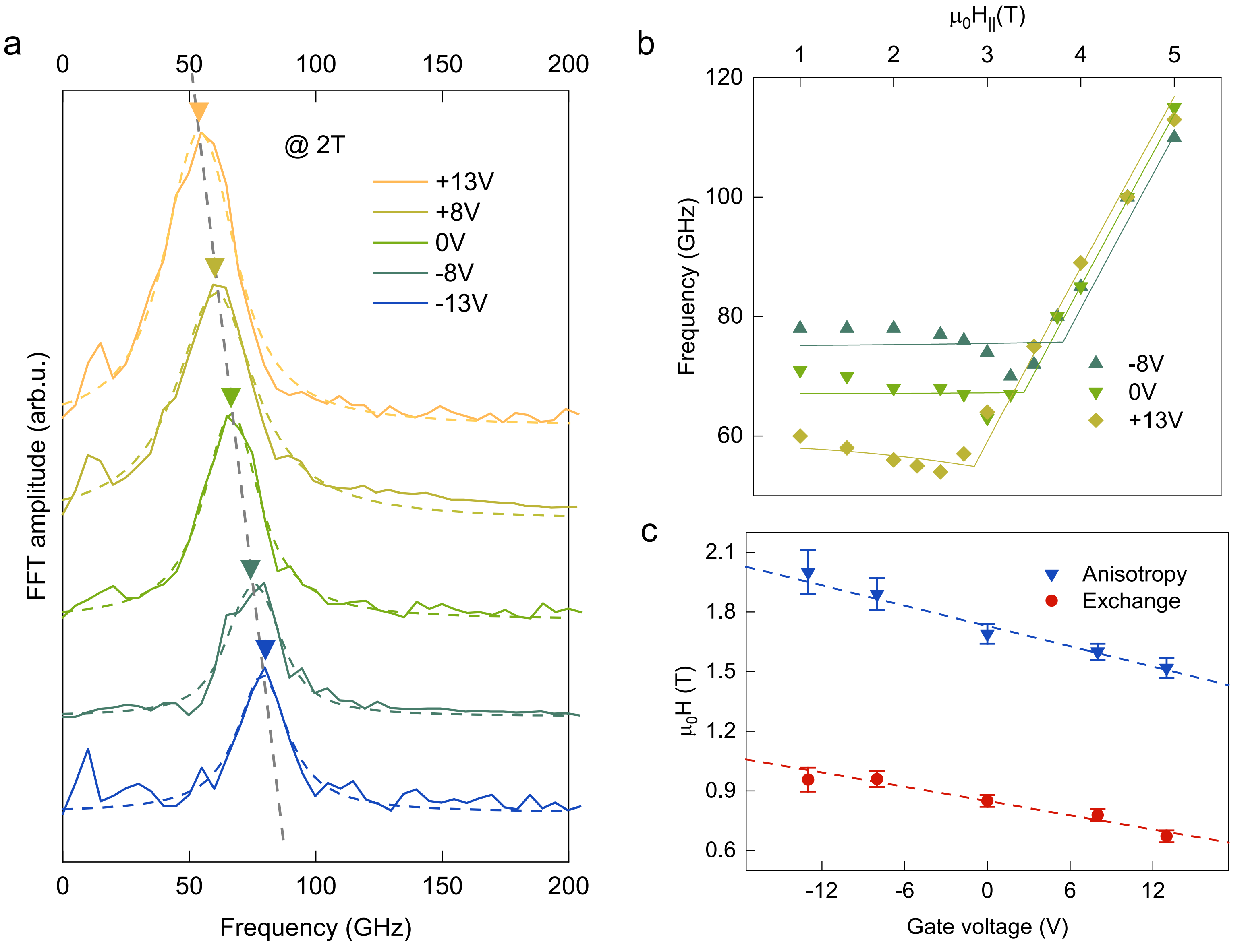

a
@ 2T
+13V
+8V
0V
-8V
-13V
FFT amplitude (arb.u.)
Frequency (GHz)
0
50
100
150
200
b
$\mu_0 H_{||}$(T)
1
2
3
4
5
Frequency (GHz)
60
80
100
120
-8V
0V
+13V
c
Anisotropy
Exchange
μ_0H (T)
0.6
0.9
1.2
1.5
1.8
2.1
-12
-6
0
6
12
Gate voltage (V)